Effects of concrete heterogeneity on FRP-concrete bond behaviour: experimental and mesoscale numerical studies

Ya-Qi Li[a], Jian-Fei Chen[b], Zhen-Jun Yang[a*], Esmaeel Esmaeeli[c], Wei Sha[d], and Yu-Jie Huang[a]

[a] Hubei Key Lab of Geotechnical and Structural Safety, School of Civil Engineering, Wuhan University, 430072, China

[b] Department of Ocean Science and Engineering, Southern University of Science and Technology, 518000, China

[c] Department of Civil and Environmental Engineering, Brunel University London, UB8 3PH, UK

[d] School of Natural and Built Environment, Queen's University Belfast, BT9 5AG, UK

*Corresponding author: zhjyang@whu.edu.cn.

Abstract

Extensive experimental and numerical studies have been conducted to understand the bond behaviour of FRP-concrete interfaces with the assumption of homogenous materials. This study is aimed at better understanding of the effects of concrete heterogeneity on the FRP-concrete bond behaviour, by a combination of experiments and mesoscale numerical modelling. FRP-concrete and FRP-mortar bonded joints were tested under a four-point bending setup. The crack initiation and propagation process with interfacial debonding until failure was accurately captured by the digital image correlation (DIC) technique. The results show that the presence of coarse aggregates in the FRP-concrete joints leads to 19% higher bond strength, but much higher variations in the bond strength and the strain distribution across the width of FRP sheets, than the FRP-mortar joints. Monte Carlo simulations of mesoscale finite element models with random distribution of polygonal aggregates were then carried out for the FRP-concrete bond tests. It is found that the distribution of coarse aggregates significantly affects the overall force-deflection responses as well as the simulated fracture processes and final failure modes that are highly comparable with the DIC observations.

Keywords: Fiber reinforced polymer (FRP); Concrete; Debonding; Finite element model; Meso-scale modelling

1. Introduction

Fiber reinforced polymers (FRP) are widely used for strengthening and retrofitting deteriorated concrete structures, typically used as sheets or laminae externally bonded to the surfaces of the upgraded elements [1]. The FRP-concrete bonded interface plays a critical role in transferring stresses from the strengthened structure to FRP [2]. Existing experimental studies show that the premature FRP-concrete interfacial debonding reduces the effectiveness of FRP strengthening significantly, and often leads to catastrophic, brittle structural failure [3].

Numerous studies have been conducted to understand and predict the FRP-concrete bond strength, both experimentally [4-8] and numerically [9-13]. Various parameters have been proved to affect the bond behaviour between FRP and concrete, including the concrete strength, the FRP axial stiffness, the bond length, and the FRP sheet to concrete width ratio. Many empirical equations have been developed by curve-fitting experimental data or through simplified analytical analyses [14-17] to predict the FRP-concrete bond strength, and some are used in structural design codes [18-20]. However, there exists a wide scatter between the values calculated from these equations [21], as well as those from different experiments (e.g. Yao et al. [7]). This may be related to the common assumption that the concrete is a homogeneous material, and thus the effects of the complex mesoscale structure of concrete such as the volume fraction, random size, shape and distribution of coarse aggregates are neglected. Extensive experiments have found that the FRP-concrete interfacial debonding usually occurs in a 2-5 mm thick layer of concrete below the FRP sheet, and in such a thin layer, the mesoscale structure of concrete should not be neglected.

Limited studies are available in the literature investigating the effects of concrete heterogeneity on the FRP-concrete bond behaviour. Using a direct shear test setup, Pan et al. [22] found that the bond capacity is heavily affected by the interfacial friction due to aggregate interlocking and the distribution and volume fraction of coarse aggregates. Barham et al. [23] conducted double-shear tests and found that both the bond strength and the maximum slip increased as the maximum aggregate size increased. Using a double-shear test setup, Mukhtar [24] found that replacing 30% normal aggregates with steel slag aggregates improved the bond performance. These limited experimental studies indicate that the mesoscale structure and composition of the concrete have significant effects on the FRP-concrete bonding performance, but more accurate, quantitative understanding of such effects is still needed, before the concrete meso-scale features can be taken into account in the design equations relations and codes.

This study aims at quantitatively clarifying the effects of meso-scale heterogeneity of coarse aggregates on the FRP-concrete bond behaviour, by a combination of comparative experiments and mesoscale nonlinear finite element simulations. A special setup of four-point bending tests is used, because the stress states are closer to those in the widely used FRP flexural strengthening of concrete beams, than the traditionally used single or double shear tests. The mortar can be seen as a homogeneous material compared with the concrete with coarse aggregates, so both FRP-concrete and FRP-mortar bond joints are tested. To accurately observe the crack initiation and propagation, the interfacial debonding and the final failure modes, the digital image correlation (DIC) technique is also applied to a few tests. In the last part of the paper, meso-scale finite element models consisting of polygonal aggregates with random shape, size and distribution are built with Monte Carlo simulations to further investigate the effect of coarse aggregate distributions on the bond behaviour, as a complement to the limited number of tests.

2. Experiments

2.1 Test setup

The modified beam test recommended by Chen et al. [25] was adopted, as shown in Fig. 1. In this test setup, a beam consisted of two separate blocks joined by two Φ12 mm steel bars at the compression side. A 409 mm long CFRP sheet with the same width as the beam was bonded to the bottom of the two blocks symmetrically with a bond length of 200 mm on both blocks. To ensure that the failure would only occur in the left block (referred to as the test block), the right block (referred to as the structural block) has a higher designed material strength, and was strengthened with 2Φ12 mm tensile bars, 3Φ8 mm stirrups, and an additional layer of 100 mm long CFRP sheet (see Fig. 1).

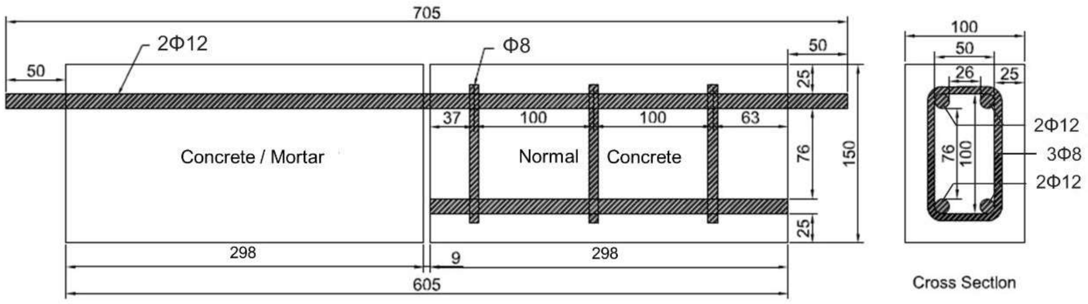

(a) Reinforcements

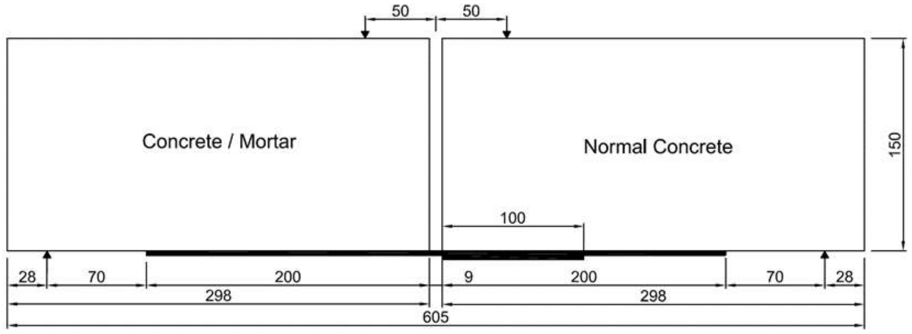

(b) FRP geometry, loading and supports

Fig. 1 Setup of the beam test (all units in mm)

Six beams were prepared and tested, including three with mortar test blocks (M-1 to M-3) and 3 with concrete test blocks (C-1 to C-3). All the structural blocks on the right are concrete. The beams were simply supported at both ends with a span of 549 mm. The loading distance is 100 mm for M-3 and 50 mm for the other five beams. The test was conducted on a Zwick machine with a load capacity of 100 kN, as shown in Fig. 2. The load was applied using a displacement control mode at a rate of 0.3 mm/min. The force in the CFRP sheet can be easily calculated from the moment equilibrium equation.

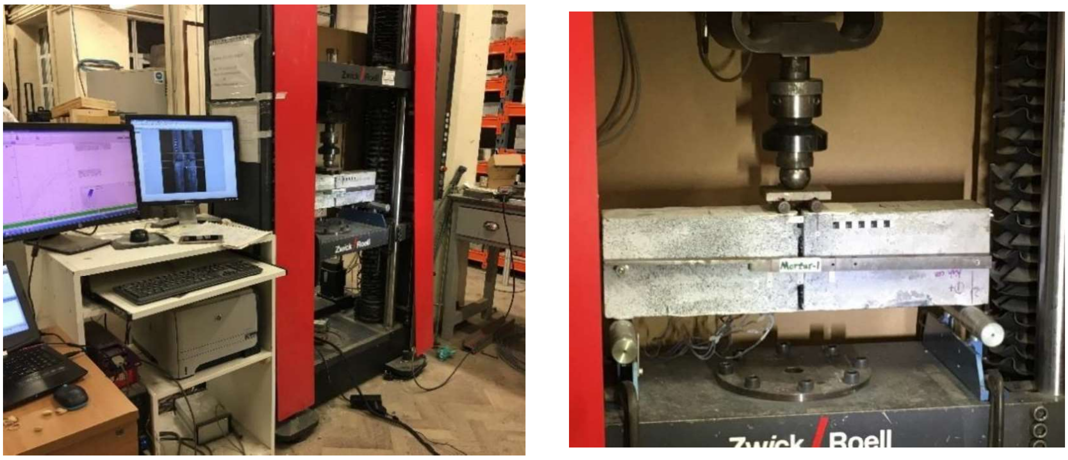

(a) Test setup (b) The beam

Fig. 2 A beam under test

2.2 Material properties

For all different concrete and mortar materials used in the blocks, six 100 mm cubes and five 200 mm × Φ100 mm cylinders were tested each under standard compression and tensile-splitting setups, respectively. The 28-day mean strengths are shown in Table 1. The characteristic yield strength of Φ6 mm and Φ12 bars was 275 MPa and 500 Mpa, respectively. The unidirectional carbon fibre sheet used was the S&P C-Sheet 240 (300 g/m^2), with a guaranteed elastic modulus of 250 GPa, a guaranteed tensile strength of 4300 N/mm^2, a rupture elongation of 1.7%, and a nominal thickness of 0.168 mm. As recommended by the manufacturer, S&P Resin Epoxy 55, a solvent-free, transparent 2-component epoxy resin with a 7-day tensile strength of 35 MPa, was used in the wet lay-up process.

Table 1. Material properties of concrete and mortar

Properties	FRP-concrete joints		FRP-mortar joints	
	Concrete (test block)	Concrete (structural block)	Mortar (test block)	Concrete (structural block)
Compressive strength (MPa)	54.0	81.0	63.0	74.0
Tensile strength (MPa)	4.45	4.75	4.30	4.60

2.3 Fabrication of specimens

Concrete and mortar blocks were cast with plywood formworks. A 9 mm thick wood plate wrapped in a cling film was placed between the two blocks to create the gap. The beams were demoulded after 24 hours and moved to a water tank for curing. After 28 days of curing, the bottom surfaces were treated using a handheld grinder to expose coarse aggregates (Fig. 3). Compressed air was then used to remove the dust to provide a clean surface for FRP bonding with the procedure illustrated in Figs 4a-d. The carbon fabrics were cut to the designed size and saturated thoroughly in the Resin Epoxy 55 bath (Fig. 4a). The surfaces of the two blocks were also saturated with the same resin (Fig. 4b). The saturated carbon fabrics were then placed on the block surfaces and pressed by a roller and a rubber spatula to remove air bubbles and evenly distribute the resin (Fig. 4c). After being cured at room temperature (20 ℃) for 7 days, the areas in contact with the loading and supporting units were carefully levelled using gypsum paste (Fig. 4d).

Fig. 3 Surface treatment

(a) FRP in the resin bath

(b) Saturating the surfaces

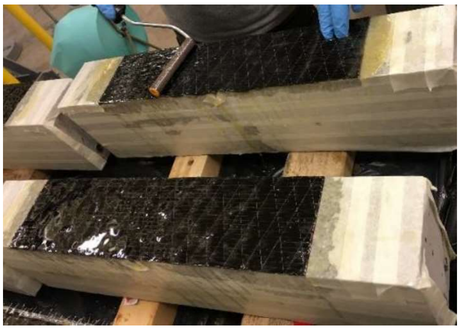

(c) Bonding the FRP sheet

(d) Levelling the loading and supporting areas

Fig. 4 Procedure of bonding FRP sheets

2.4 Data acquisition and DIC tests

For each beam, nine 6 mm TML FLAB-6-11 strain gauges (SGs) were installed. Five were installed on the centreline of the FRP sheet bottom to measure the longitudinal FRP strain distribution, as shown in Fig. 5. The four remaining SGs were installed along the width of the FRP sheet at the same longitudinal location as the second SG to measure the transverse strain distribution. The SGs were connected to a data logger recording the strains every 0.5 seconds.

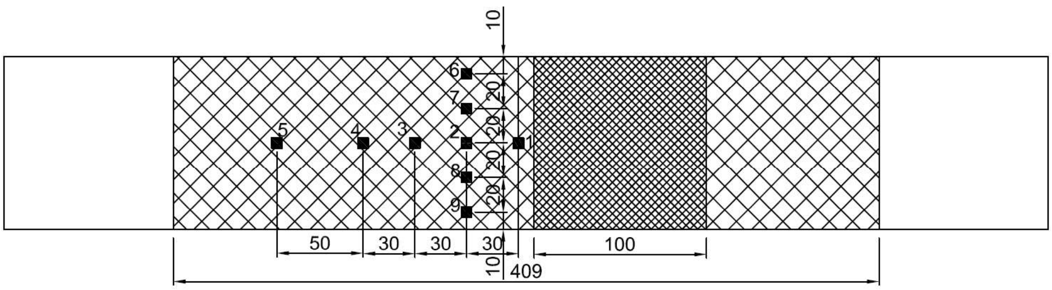

Fig. 5. Locations of the strain gauges

For specimens C-2, C-3 and M-1, the DIC technique was used to measure the displacement and strain fields and observe the crack initiation and propagation process. The test block was painted with white spray followed by a black mist paint to create random speckles (Fig. 6). The setup for DIC measurements comprised a high-resolution digital camera (Canon EOS 5D Mark III) and a normal white light to provide uniform light intensity across the surface. The camera was placed perpendicular to the specimen surface, capturing digital images every 0.3 s with a resolution of 681×1023 pixels in a field of view of 283 mm×425 mm. The displacement and strain fields were computed using an open-source DIC software GOM Correlate [26].

A few target points (TPs) were also adhered to the specimen (Fig. 6) and their DIC displacements were used to calculate the deflection and to compare with the numerical results. The displacements may be affected by the rigid movement of supports, the deformation of the gypsum paste, the possible rotation of the specimen, etc., and cannot be treated as the true deflection. A steel yoke was thus fixed at the mid height of the beam, with a pin connection at one end and a rolling connection at the other and both vertically above the supports. The relative vertical displacement between TP1 and TP3 or between TP2 and TP3 was then treated as the true deflection.

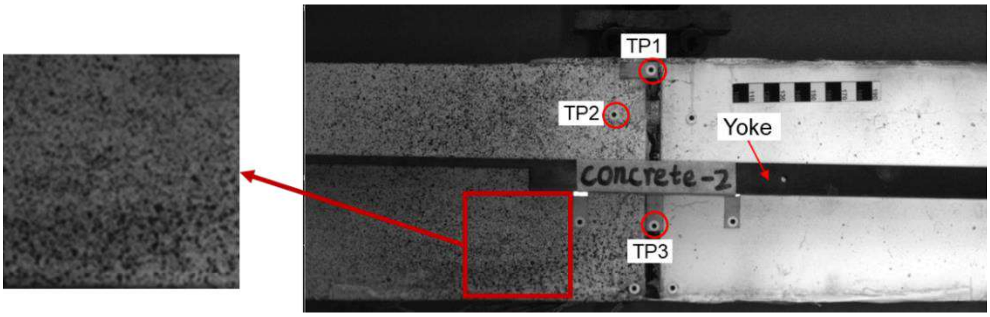

Fig. 6 Random speckle pattern using paint for DIC

3. Test results and analysis

3.1 Load-deflection responses and failure modes

Fig. 7 compares the DIC-measured displacements and deflections at the points TP1 and TP2 of two specimens (C-2 and M-1). It can be seen that using the steel yoke can effectively remove the displacements introduced by the other factors to obtain true deflections. The deflections at TP2 will be used in the force-deflection curves and for comparison with the numerical results as follows.

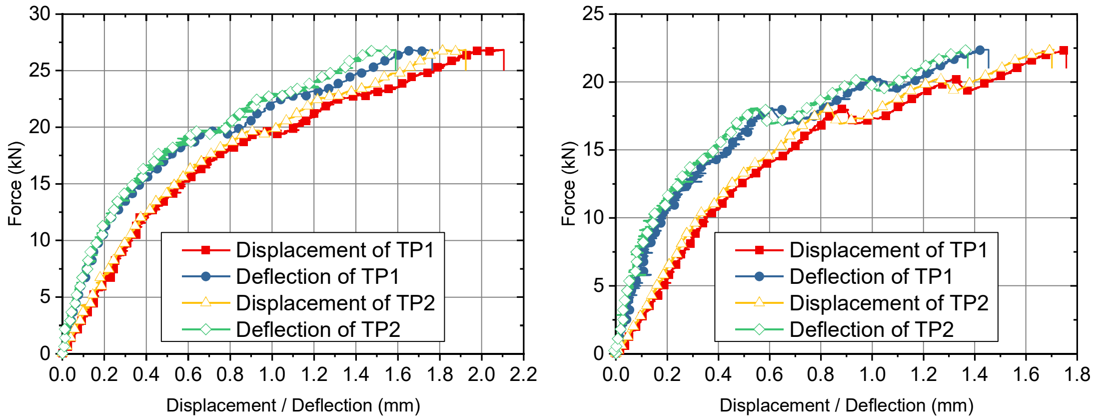

(a) C-2 (b) M-1

Fig. 7 Comparsion of displacements and deflections from DIC analyses

The force – deflection curves of all the tested specimens are shown in Fig. 8. It can be seen that the force first increases almost linearly as the displacement with almost the same slopes for the three repeated tests. A further increase in the deflection is accompanied by a reduction of the beam's stiffness, indicating the initiation of micro-cracks. As the cracks propagate and widen, the stiffness continues to decrease, until a "snap" was heard and the ultimate brittle failure happened, in all the test blocks (Fig. 9). The failure was characterised with CFRP sheet debonding induced by the development of a major intermediate shear crack (DB-IC failure) near the mid-span in the five beams, except in M-1 where an additional crack initiated from the bonded end of the CFRP sheet, propagated towards the loading point and led to the sudden failure (BF), following the intermediate shear crack propagation. In the DB-IC failure modes, it can be seen that a thin layer of concrete/mortar were attached to the CFRP sheet near the debonding end, as observed in many other joint tests, which indicated that the debonding failure indeed occurred in the weakest concrete/mortar substrates.

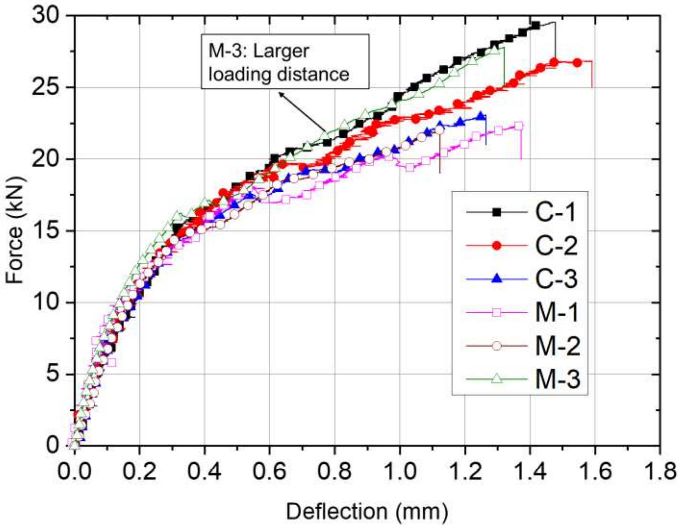

Fig. 8 Force versus displacement responses of six beam tests

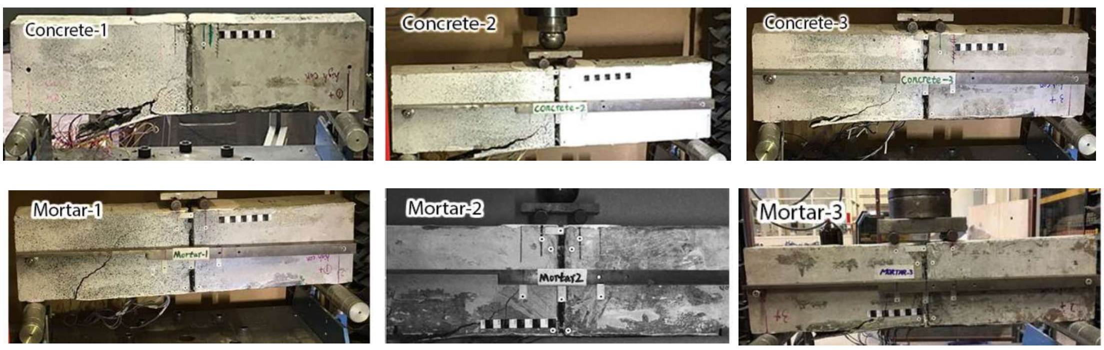

Fig. 9 Failure modes of the tested specimens

Table 2 summarises the results of all the six tests. The major intermediate cracks in all the specimens initiated at 75-135 mm from the gap with an angle of 30 or 45^{o} . The deflection and peak force upon failure varied from 1.11-1.62 mm and 22.0-29.6 kN, respectively. This indicates the good reproducibility of the tests. It can be seen that the mean force in the CFRP sheet of the three concrete-FRP joints is about 19% higher than that in the mortar-FRP joints. There are two reasons for this. Firstly, the concrete surface after grinding was more uneven and more epoxy resin penetrated into the concrete, leading to higher interfacial bond properties between the CFRP and the concrete substrate than in the FRP-mortar joints. Another reason may be the coarse aggregate interlocking in the concrete that led to higher fracture resistance, higher interfacial friction and thus higher bond strength. The coefficient of variation (CoV) of the FRP forces in concrete joints were 7 times that in the mortar joints, which should again be attributed to the much more heterogeneous mesoscale structure of concrete due to random distribution of coarse aggregates than the homogeneous mortar material.

Table 2 Summary of the test results

Test	C-1	C-2	C-3	M-1	M-2	M-3
Peak Force (kN)	29.6	26.8	23.1	22.4	22.0	27.8
Displacement at failure (mm)	1.48	1.59	1.26	1.37	1.12	1.32
Distance between the loading point and the left support (mm)	224.5	224.5	224.5	224.5	224.5	174.5
Distance between the steel bars and the CFRP sheet (mm)	120.53	120.91	119.66	118.50	118.98	118.25
Force in CFRP sheet (kN)	27.57	24.88	21.67	21.22	20.75	20.51
Average force in CFRP sheet (kN)		24.71			20.83	
CoV of force in CFRP sheet (kN)		11.9%			1.7%	
Failure mode	DB-IC	DB-IC	DB-IC	BF	DB-IC	DB-IC

Note: (a) The distance between two loading points is 50mm except for M-3 (100 mm) (b) DB-IC: intermediate-crack induced debonding failure; BF: block failure.

3.2 Strain distribution along the FRP sheet

The FRP longitudinal strain distributions of all the specimens at different load levels, measured by the five SGs (Fig. 5), are plotted in Fig. 10. The load level was defined as the percentage of the current load over the ultimate load. At load levels lower than 50%, the bonded joint was under elastic stage, the strain in the FRP sheet decreased quickly with the distance from the middle gap. This is the well-known shear-lag effect, and the rapid drop is due to the much smaller stiffness of the FRP sheet with respect to that of the concrete/mortar substrate [22]. After the load reached about 50%-60% of the peak load, micro-cracks started to initiate around the mid-span of specimens and the length of FRP sheet with higher strains extended rapidly. Beyond this stage, the length experiencing strains continued to increase, accompanied with gradual changing in the concavity of the strain profiles for most specimens. The interfacial debonding zone propagated to the far/free end of the FRP sheet, as indicated by the shifting of strain distribution towards the free end. The sudden increase of strain coincides with crack initiation or propagation to the SG position, through the DIC analyses of the failure process. For example, the reading of SG near the free end of C-1 suddenly increased when the load reached 90% of the ultimate load, indicating that the debonding crack propagated to the SG position (Point E in Fig. 13). Similarly, at the ultimate load, the reading of SG5 of M-1 underwent abrupt increase, due to the sudden appearance of the shear crack from the free end of FRP sheet, as presented in Fig. 14.

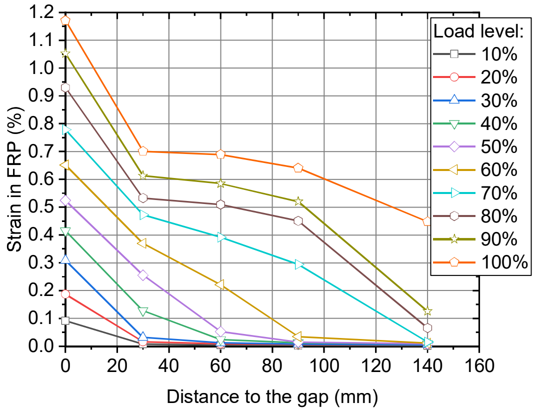

(a) C-1

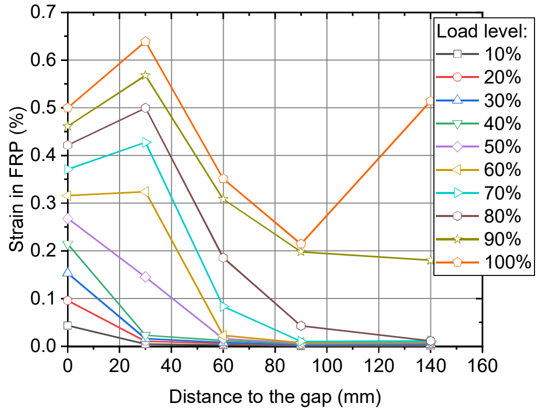

(d) M-1

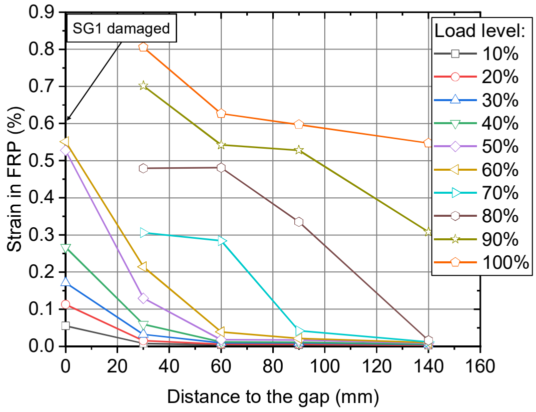

(b) C-2

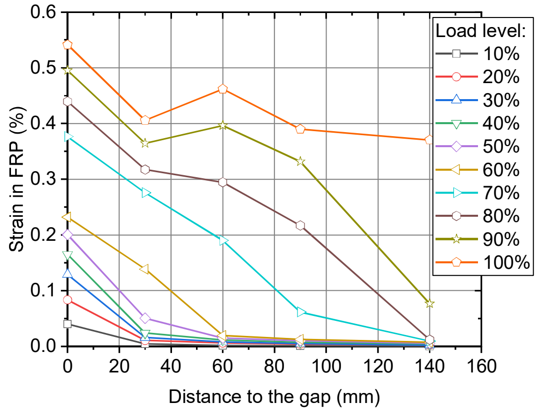

(e) M-2

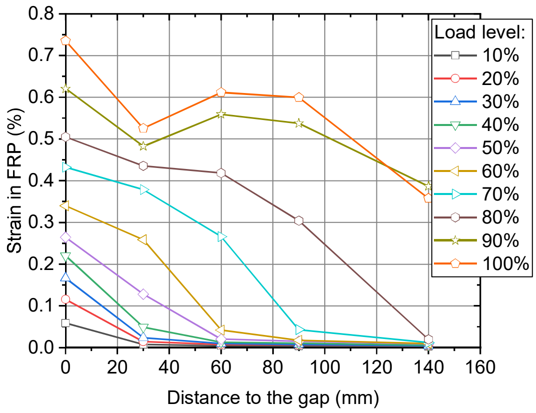

(c) C-3

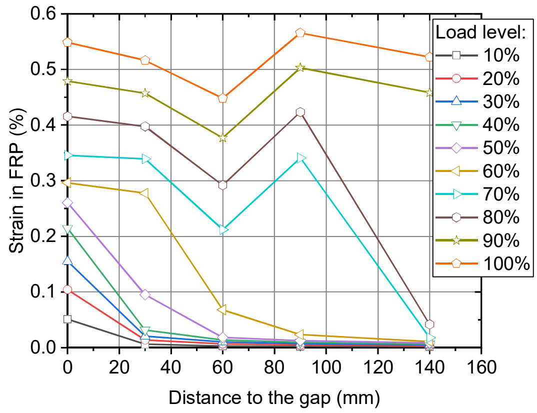

(f) M-3

Fig. 10 Strain distributions along the FRP sheet at different load levels

3.3 Strain variation across the FRP width

Fig. 11 compares the distributions of strain across the FRP width at different load levels for C-2 and M-2, respectively, as examples. It can be seen that the strain distribution in C-2 was generally more scattered than that in M-2. This phenomenon was more evident at lower load levels (from 10% to 30%) where the tested specimens were still largely elastic without macro cracks. Again, this should be caused by the higher mesoscale heterogeneity in the concrete than in the mortar.

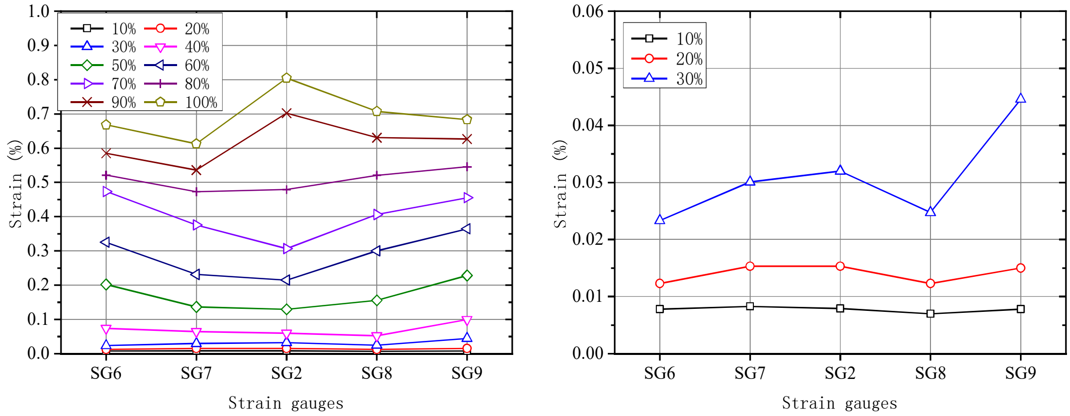

(a) C-2

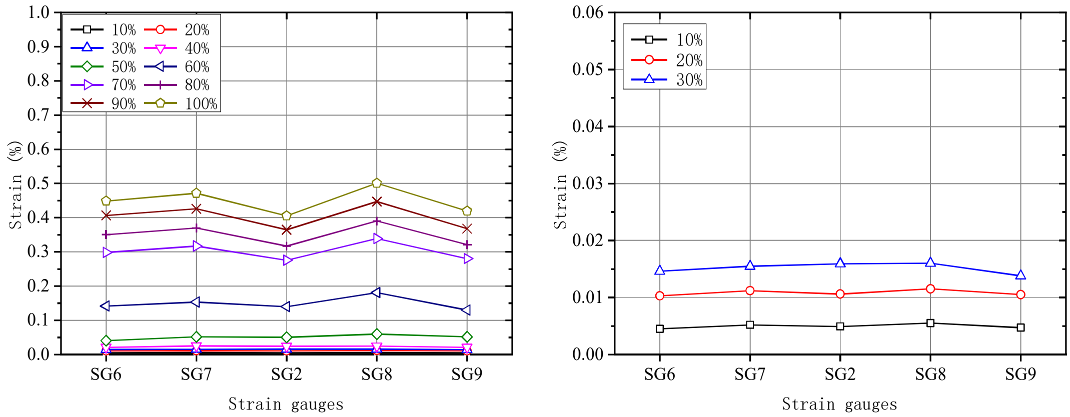

(b) M-2

Fig. 11 Strain profiles across the width at different load levels at whole (left) and low (right) load levels

The CoV of strain distribution at each load level was then calculated for all six specimens. The average values are presented in Fig. 12. The variation of the strain distribution across the width of the FRP in the FRP-concrete joints is generally higher than that of the FRP-mortar joints. The average COVs up to 30% load of the three FRP-concrete beams is 15.7%, whereas that of the three FRP-mortar beams is only 7%.

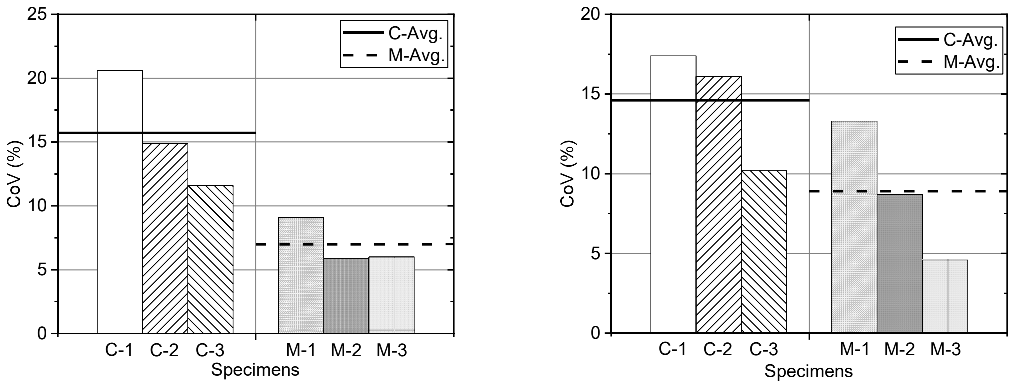

(a) Up to 30% of the peak load (b) Up to the peak load

Fig. 12 Average CoV of strain distribution of six specimens

3.4 Failure process from DIC analysis

The failure process of FRP-concrete joint C-3, and FRP-mortar joint M-1 were presented in Fig. 13 and Fig. 14, respectively. Only the test block of each specimen was shown. For C-3, a flexural-shear crack firstly initiated near the middle gap of the specimen. As the load increases, more flexural-shear cracks appeared near the FRP bonded interface and developed towards the mid-height of the specimen. Then some of the micro-cracks connected and propagated parallel to the FRP sheet and adjacent to the FRP-concrete interface, towards the free end of the FRP sheet, resulting in full debonding of the FRP. The failure process of M-1 at the early stage is similar to that of C-3, whereas a shear crack starting from the FRP end suddenly occurred and led to the very brittle splitting of the mortar block before full debonding of the FRP sheet. Through the DIC tests, some cracks which are impossible to be seen at the early loading stage, can be easily captured.

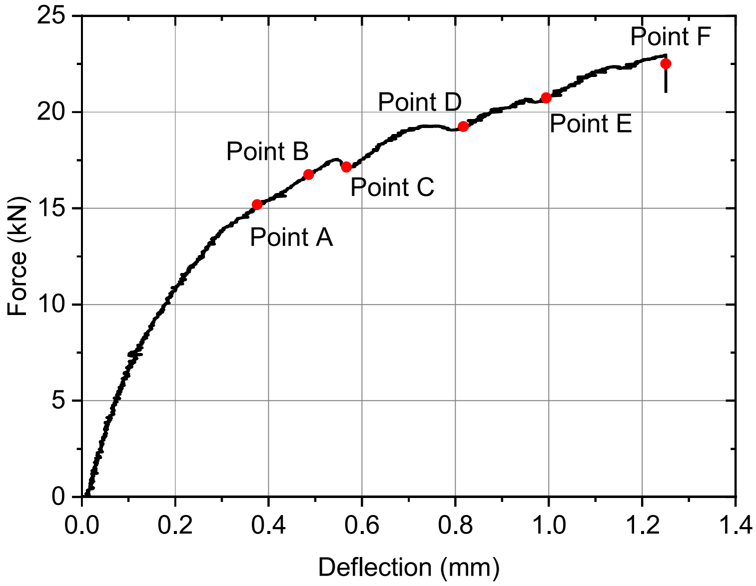

(a) Force-deflection curve

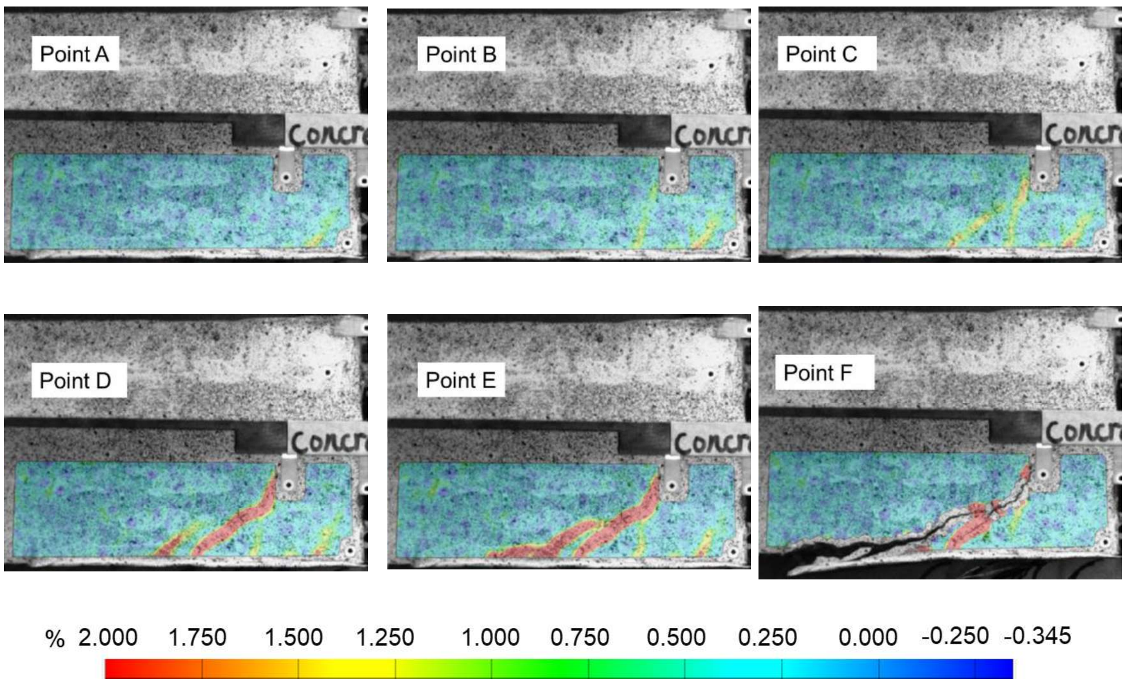

(b) Failure process

Fig. 13 Behaviour of FRP-concrete joint C-3

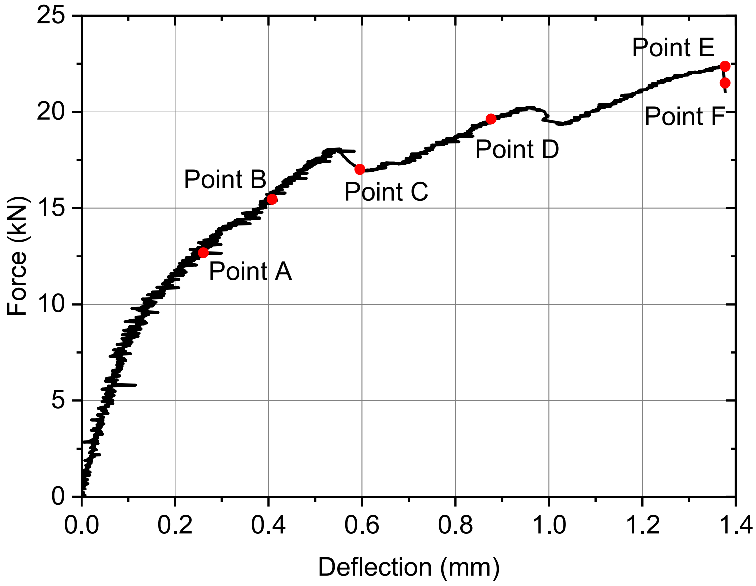

(a) Force-deflection curve

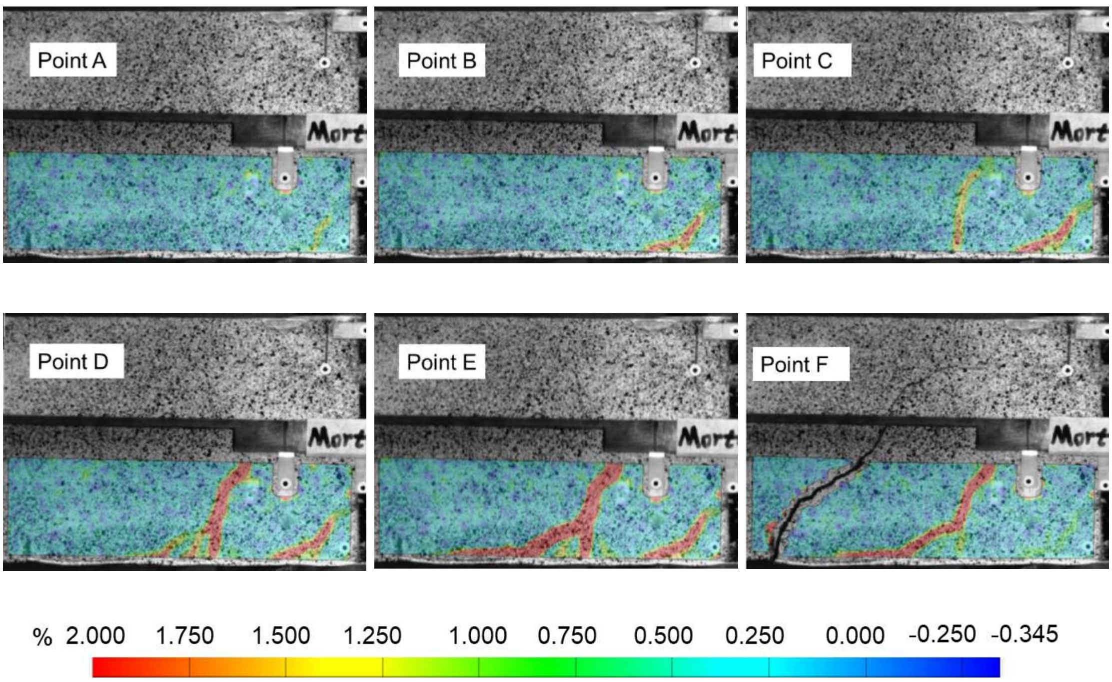

(b) Failure process

Fig. 14 Behaviour of FRP-mortar joint M-1

4. Mesoscale numerical analysis

The above experimental studies have demonstrated the qualitative effects of concrete heterogeneity on the strain distribution and complicated failure behaviour of FRP-concrete joints but the number of tests is quite limited. To quantitatively investigate the effects of the concrete heterogeneity, meso-scale FE models with random distribution of aggregates are then simulated.

4.1 Generation of mesoscale models and finite element meshes

Fig. 15 shows a 2D multiscale FE mesh for the beam test. To limit the computational cost, only a zone of 80 mm * 205 mm above the bonding line was modelled with mesoscale random aggregates, while the rest of the beam was assumed homogeneous. The element size was typically 1 mm in the mesoscale zone and 2 mm in other parts with 4-noded plane stress elements (CPS4). In the mesoscale zone, coarse aggregates are randomly embedded in the mortar matrix. A take-and-place algorithm [27-29], implemented in MATLAB and Python codes, was used to generate random aggregates. The volume fraction of coarse aggregates in the beam tests was about 41%, and the characteristic size is 20 mm, 10 mm and 6 mm with a 6:2:1 volume ratio. The same coarse aggregate volume distribution and sizes were adopted in the mesoscale modelling zone.

The FRP was assumed as an isotropic linear elastic material and modelled by CPS4 elements. The average thickness of FRP laminates formed from the wet lay-up process was t_p =1.22 mm. The Young's modulus was set as E_p = 33 GPa so that its axial rigidity E_pt_p remains the same as the dry FRP sheet. Its Poisson's ratio was assumed as 0.3. The steel reinforcement bars, with Young's modulus of 200 GPa and Poisson's ratio of 0.3, were simplified as elastic material as they were far away from the FRP bonding line and did not yield until failure. They were modelled by 2-noded linear truss elements (T2D2). The material properties for the homogeneous concrete can be found in Section 2.2. Both the FRP sheet and the steel reinforcement bars were assumed to be perfectly bonded to the surrounding concrete using the TIE command in ABAQUS.

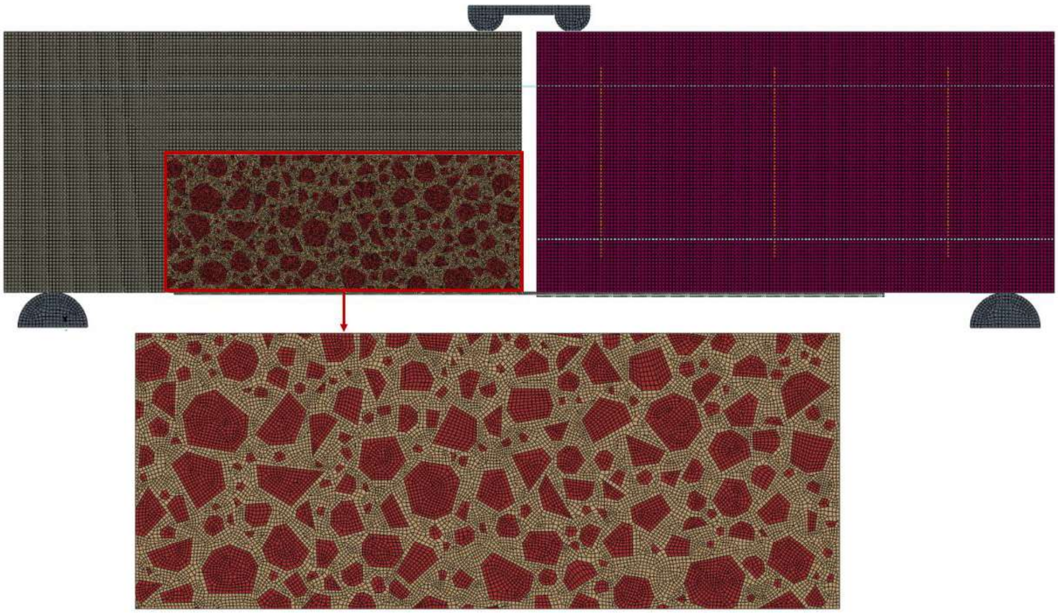

Fig. 15 Multiscale FE model of the FRP-concrete beam test

4.2 Material properties and constitutive models for meso-components of concrete

For normal strength concrete, the uniaxial cylinder compressive strength of coarse aggregates $f_a^{'}$ ranges from 80 (for limestones) to 100MPa (for basalt). Herein $f_a^{'}$=100MPa are used for all the simulations, and its cubic compressive strength is f_a=122.63 MPa, adopted from the experimental results of typical crushed basalts [30]. The Young's modulus E_a can be estimated according to the concrete code Eurocode 2 [31] as

$$E_a = 22(f_a/10)^{0.3} \tag{1}$$

Then the Young's modulus of mortar E_m can be calculated from the Mori-Tanaka homogenisation theory [32,33]

$$E_c = E_m + \frac{V_a(E_a - E_m)}{1 + (1 - V_a)\frac{E_a - E_m}{E_m + 4\mu_m/3}} \tag{2}$$

where E_c is the Young's Modulus of concrete, which is calculated by Eq. 1 with the cubic compressive strength of concrete f_c =54 MPa. V_a is the volume fraction of coarse aggregates; $\mu_m = \frac{E_m}{2(1+\nu_m)}$ is the shear modulus of the mortar; and $\nu_m = 0.2$ is Poisson's ratio of the mortar.

The cylinder compressive strength of mortar $f_m{}'$ is then evaluated according to the experimental relationship proposed by Sideris et al. [34]

$$f_m' = (E_m - 12.4147)/0.2964 \tag{3}$$

The basic tensile properties are calculated according to CEB-FIP [35]. The uniaxial tensile strength f_t, for the homogeneous concrete and coarse aggregates is calculated

$$f_t = 1.4\left(\frac{f_c' - 8}{10}\right)^{\frac{2}{3}} \tag{4}$$

where $f_c{}'$ is the cylinder strength of concrete and coarse aggregates. For normal strength concrete, $f_c{}'$ can be estimated from $f_c' = f_c * 0.79$ according to BS 8110 [36].

The lower bound value of this model is used for the mortar considering its normally lower tensile strength than concrete

$$f_t = 0.95\left(\frac{f_m' - 8}{10}\right)^{\frac{2}{3}} \tag{5}$$

The fracture energy G_f is

$$G_f = (0.0469 d_a^2 - 0.5 d_a + 26)\left(\frac{f_c'}{10}\right)^{0.7} \tag{6}$$

where d_a is the maximum aggregate size. In this study, d_a is assumed to be 2.36 mm [37] when calculating G_f for the mortar. The maximum fracture energy (0.205 N/mm) for C100 concrete in CEB-FIP [35] was adopted for coarse aggregate considering that there is no conventional model for aggregates in the concrete.

Table 3 shows all the material properties for the coarse aggregates and the mortar in this study.

Table 3. Material parameters for the meso-components of concrete for FRP-concrete joints

	Elastic modulus (GPa)	Cylinder compressive strength (MPa)	Tensile strength f_t (MPa)	Fracture energy G_f(N/mm)
Aggregate	46.7	100	6.15	0.205
Mortar	30.8	62	2.92	0.090

Both the coarse aggregates and the mortar in the mesoscale zone were modelled using the concrete damage plasticity (CDP) model available in ABAQUS, which has been proved capable of modelling concrete damage and fracture leading to FRP-concrete debonding in macroscopic FE models [9,38], and modelling the damage and fracture of concrete at the mesoscale [39,40].

For uniaxial tensile behaviour in the CDP model, the stress (σ_t) - crack opening displacement (w_t) relationship proposed by Hordijk [41] is adopted to minimise mesh dependence of results

$$\frac{\sigma_t}{f_t} = \left[1 + \left(c_1 \frac{w_t}{w_{cr}}\right)^3\right] e^{\left(-c_2 \frac{w_t}{w_{cr}}\right)} - \frac{w_t}{w_{cr}}(1 + c_1^3)e^{-c_2} \tag{7}$$

$$w_{cr} = 5.14 \frac{G_f}{f_t} \tag{8}$$

where w_{cr} is the crack opening displacement at the complete loss of tensile stress, and $c_1 = 3.0$ and $c_2 = 6.93$ are constants determined from tensile tests.

The uniaxial compressive stress (σ_c) – strain (ε_c) behaviour is described by the following stress-strain relationship proposed by Nakamura and Higai [42]

$$\sigma_c = f_c' \left[\frac{2\varepsilon_c}{\varepsilon_p} - \left(\frac{\varepsilon_c}{\varepsilon_p} \right)^2 \right] \quad (0 \le \varepsilon_c \le \varepsilon_p)$$

$$\sigma_c = (\varepsilon_c - \varepsilon_u)/(\varepsilon_u - \varepsilon_p) \quad (\varepsilon_p \le \varepsilon_c \le \varepsilon_u) \tag{9}$$

where σ_p and ε_p are the experimentally determined maximum stress and its corresponding strain; and $\varepsilon_u = \frac{2G_c}{(f_c' \mathrm{L})} - \varepsilon_0$. L is the element size and $\varepsilon_0 = \varepsilon_p/2$. G_c is the compressive fracture energy [43-46], which is assumed as 100 times the tensile fracture energy G_f.

The damage evolution behaviour under uniaxial tension or compression is modelled by Lubliner et al. [47]

$$\mathrm{d} = 1 - \frac{\sigma}{f} \tag{10}$$

in which σ is the stress and f is either the tensile or compressive strength as appropriate.

4.3 Results and discussion

4.3.1 Force-deflection responses

Monte Carlo simulations of 20 multiscale models with different distributions of coarse aggregates were carried out. The predicted force-deflection curves and the mean curve are shown in Fig. 16, compared with the test results of C-1, C-2 and C-3. It can be seen that the Monte Carlo results largely cover the three test results, indicating the FE modelling approach is appropriate for simulating the nonlinear debonding behaviour of the FRP-concrete joints. However, considerable scatters can be seen in the ultimate force and the maximum deflection for both the 20 FE models and the 3 tested specimens, which are summarised in Table 4. The ultimate forces and maximum deflection from the Monte Carlo simulations range from 23.1 kN to 32.5 kN, and 1.18 mm to 1.70 mm, respectively. The mean values are 27.2 kN and 1.38 mm, which are close to the test results of 26.5 kN and 1.44 mm, respectively. The coefficient of variation (CoV) for the ultimate force and the maximum deflection are 10.4% and 12.3%, and 12.3% and 14.1% for the FE simulations and the test, respectively. These findings demonstrate again that the concrete heterogeneity (random distribution of coarse aggregates) significantly affects the loading capacity of the FRP-concrete joints.

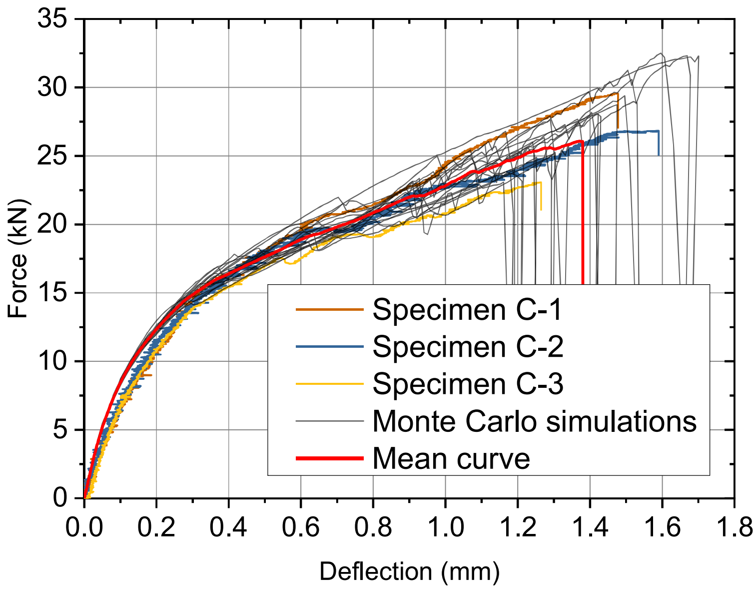

Fig. 16 Predicted force-deflection curve of 20 Monte Carlo simulations

Table 4 Statistic comparison of Monte Carlo simulations and test results

	Monte Carlo simulations		Test	
	Ultimate Force (kN)	Maximum deflection (mm)	Ultimate force (kN)	Maximum deflection (mm)
Minimum value	23.1	1.18	23.1	1.26
Maximum value	32.5	1.70	29.6	1.59
Average value	27.2	1.38	26.5	1.44
CoV	10.4%	12.3%	12.3%	11.6%

4.3.2 Predicted failure process

Two typical failure processes were observed in the 20 FE models, as shown in Fig. 17 and Fig. 18, respectively. In both cases, the damage initiated in the mortar surrounding the coarse aggregates near the middle gap. With the increase of loading, more flexural and flexural-shear cracks (the elements with high tensile damage index herein) initiated near the bonding line and propagated towards the loading point, and newly-formed short cracks were merged into the existing cracks in the mortar. Meanwhile, FRP-concrete interfacial debonding occurred at the toes of major cracks. In the Type I failure mode, the model failed with one dominant flexural-shear crack propagating towards the loading point and the simultaneous interfacial debonding towards to bonding end, which is consistent with the typical IC debonding the DIC test observations (Fig. 13). The Type II failure process was similar to the Type I, except that after the ultimate force was reached, an additional shear crack suddenly initiated at the bonding end and fast propagated towards the loading point, resulting in the very brittle failure. The predicted failure process and the final failure mode are similar to those of the tested specimen M-1 (Fig. 14).

Mechanically, there exists local stress concentration at the right-angled corner of FRP-bonded joints at the bonding end, which tends to initiate an inclined crack propagating towards the loading point, and often leads to premature failure characterised with concrete cover separation in flexurally strengthened beams [1,12]. The zoomed-in region near the bonding end at the failure point F is also shown in Fig. 17 and Fig. 18 for the Type I and Type II failure mode, respectively. It can be seen that in the first case, the inclined crack caused by local stress concentration was forced to propagate upwards and then the propagation was stopped, due to the obstruction of a big aggregate at the bonding end, whereas in the second case, the inclined crack was able to extend in the mortar between two small aggregates and subsequently propagate towards the loading end. This indicates that both the morphologies (size, shape and orientation etc.) of the coarse aggregates and their distribution near the bonding end play an important role in the forming of final failure modes.

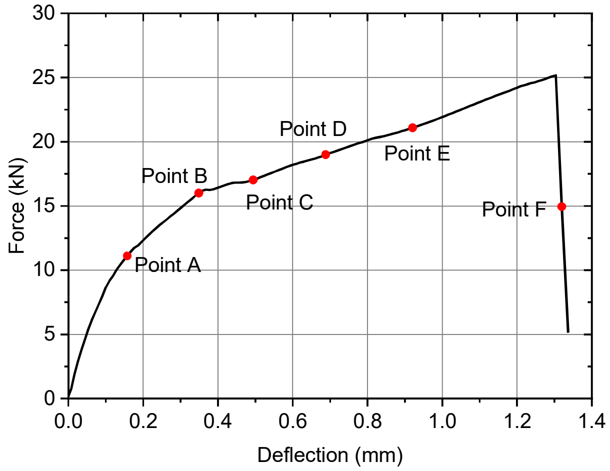

(a) Force-deflection curve

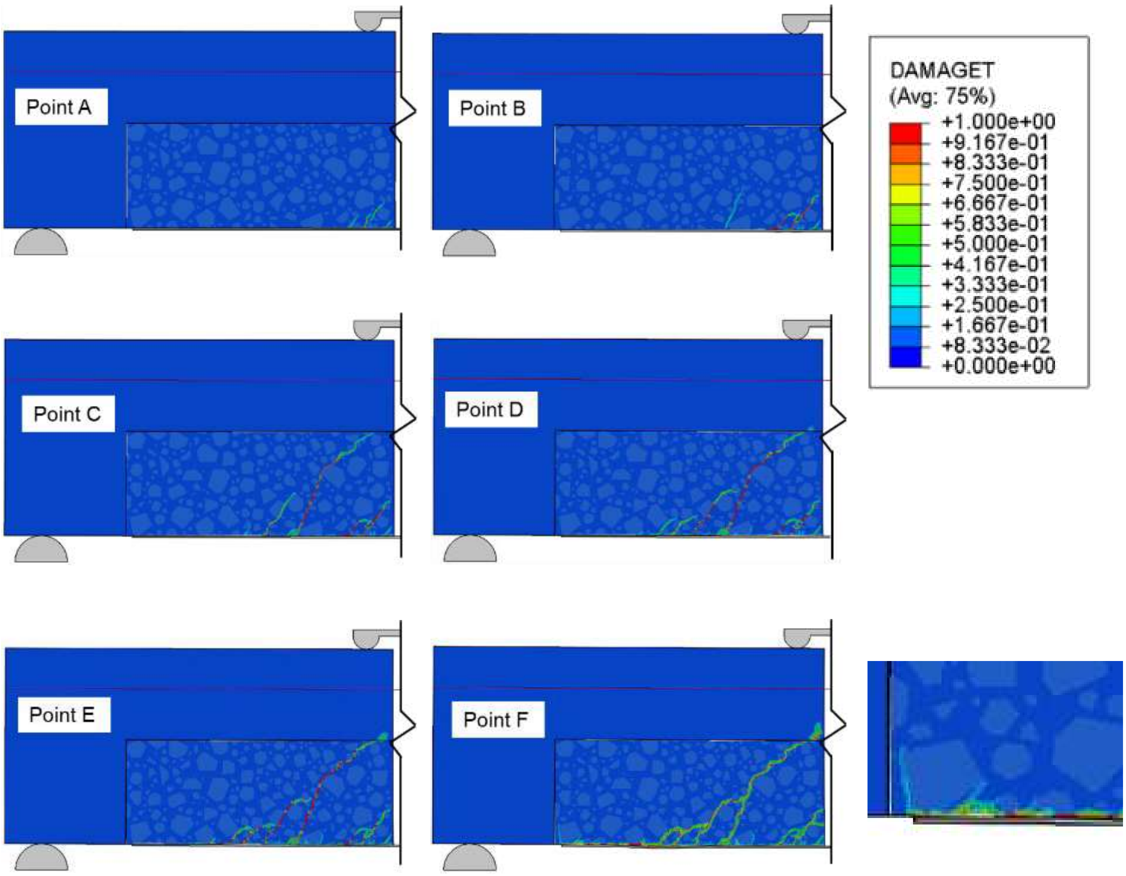

(b) Failure process

Fig. 17 Typical Type I failure process simulated by a multiscale FE model: the final figure shows a zoomed region near the bonding end at the point F

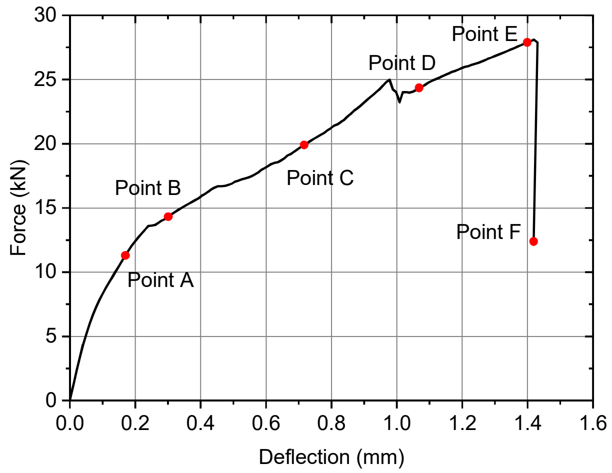

(a) Force-deflection curve

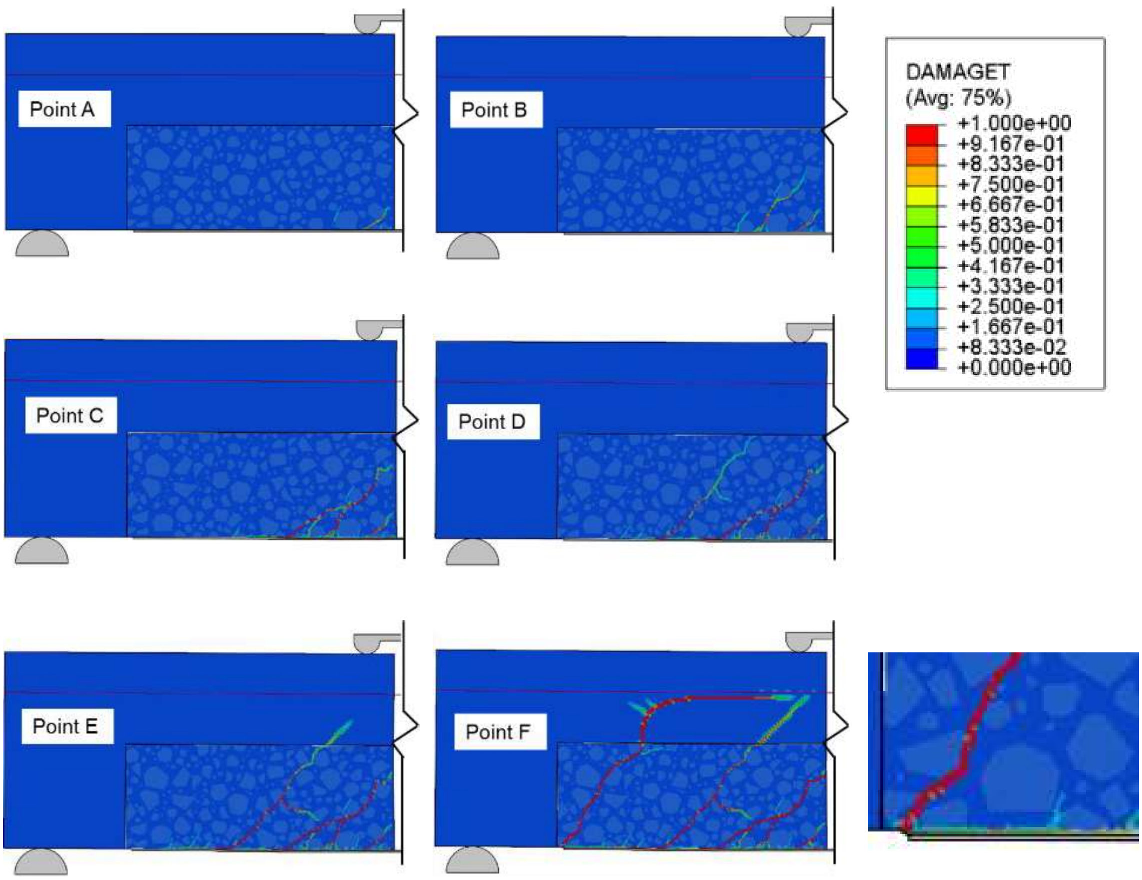

(b) Failure process

Fig. 18 Typical Type II failure process simulated by a multiscale FE model: the final figure shows a zoomed region near the bonding end at the point F

5. Conclusions

In this paper, the effects of concrete material's heterogeneity on the mechanical behaviour of FRP-concrete bonded joints have been studied by a combination of experiments and mesoscale finite element simulations. The main conclusions are:

(1) Six FRP-concrete and FRP-mortar bonded joints were tested under a four-point bending setup, with crack initiation and propagation processes until failure accurately captured by the DIC technique. It has been found that, the mean peak force of the FRP-concrete joints is about 19% higher than that of FRP-mortar joints, due to the higher interfacial friction and improved epoxy resin penetration into the uneven surface of concrete after treatment. However, the CoV of the mean peak force in the former specimens is 7 times that of the latter. Meanwhile, the variation in the strain distribution across the width of the FRP sheet in the FRP-concrete bonded joints is more than 2 times that in the FRP-mortar bonded joints.

(2) The DIC study shows that there exist two distinct failure modes in the beam test setup: the flexural-shear crack induced FRP debonding and the brittle block splitting from the FRP bonding end.

(3) Multiscale FE models of the bending tests are built with the region of interests above the bonding line simulated by mesoscale composition with randomly distributed coarse aggregates generated by a take-and-place procedure. Monte Carlo simulations of 20 models show that the distribution of coarse aggregates significantly affects the peak force and the maximum deflection, with CoV up to 10.4% and 12.3%, respectively. The mesoscale heterogeneity (both the morphologies such as size, shape and orientation of coarse aggregates and their distribution) also plays a significant role in the forming of two distinct final failure modes that are highly consistent with the DIC results.

(4) The mesoscale FE simulations, after careful calibration and validation against experiments, are promising to supplement the limited laboratory tests for development of more accurate

strength equations of FRP-concrete bonded joints, considering other heterogeneity-related parameters such as the gradation and shapes of coarse aggregates.

Acknowledgements

This study is funded by National Natural Science Foundation of China (No. 51974202 and No. 51779222), Key Research and Development Programme of Hubei Province (No. 2020BAB052), and Sino-German Center for Research Promotion (Mobility Programme No. M-0172).

Data Availability Statement

All data generated or analyzed during this study are included in this article.

References

[1] Teng JG, Chen JF, Simth ST, Lam L. FRP-strengthened RC structures. Chichester: Wiley; 2002.

[2] Ueda T, Dai J. Interface bond between FRP sheets and concrete substrates: properties, numerical modeling and roles in member behaviour. Prog Struct Eng Mater 2005;7:27–43.

[3] Kang THK, Howell J, Kim S, Lee DJ. A State-of-the-Art Review on Debonding Failures of FRP Laminates Externally Adhered to Concrete. Int J Concr Struct Mater 2012;6:123–34.

[4] De Lorenzis L, Miller B, Nanni A. Bond of FRP laminates to concrete. ACI Mater J 2001;98:256–64.

[5] Gartner A, Douglas EP, Dolan CW, Hamilton HR. Small beam bond test method for CFRP composites applied to concrete. J Compos Constr 2010;15:52–61.

[6] Tatar J, Hamilton HR. Comparison of laboratory and field environmental conditioning on FRP-concrete bond durability. Constr Build Mater 2016;122:525–36.

[7] Yao J, Teng JG, Chen JF. Experimental study on FRP-to-concrete bonded joints. Compos Part B Eng 2005;36:99–113.

[8] Ali-Ahmad M, Subramaniam K, Ghosn M. Experimental investigation and fracture analysis of debonding between concrete and FRP sheets. J Eng Mech 2006;132:914–23.

[9] Tao Y, Chen JF. Concrete damage plasticity model for modeling FRP-to-concrete bond behavior. J Compos Constr 2015;19:4014026.

[10] Chen GM, Teng JG, Chen JF. Finite-element modeling of intermediate crack debonding in FRP-plated RC beams. J Compos Constr 2011;15:339–53.

[11] Lu XZ, Ye LP, Teng JG, Jiang JJ. Meso-scale finite element model for FRP sheets/plates bonded to concrete. Eng Struct 2005;27:564–75.

[12] Yang ZJ, Chen JF, Proverbs D. Finite element modelling of concrete cover separation failure in FRP plated RC beams. Constr Build Mater 2003;17:3–13.

[13] Lin J, Wu Y, Smith ST. Width factor for externally bonded FRP-to-concrete joints. Constr Build Mater 2017;155:818–29.

[14] Chen JF, Teng JG. Anchorage strength models for FRP and steel plates bonded to concrete. J Struct Eng 2001;127:784–91.

[15] Lu XZ, Teng JG, Ye LP, Jiang JJ. Bond–slip models for FRP sheets/plates bonded to concrete. Eng Struct 2005;27:920–37.

[16] Camli US, Binici B. Strength of carbon fiber reinforced polymers bonded to concrete and masonry. Constr Build Mater 2007;21:1431–46.

[17] Khalifa A, Gold WJ, Nanni A, M.I. AA. Contribution of Externally Bonded FRP to Shear Capacity of RC Flexural Members. J Compos Constr 1998;2:195–202.

[18] CEB-FIP. Externally bonded FRP reinforcement for RC structures. Bulletin No. 14, 2001; fib

[19] ACI 440.2R-17. Guide for the design and construction of externally bonded FRP Systems for strengthening concrete structures. Farmington Hills, MI, USA: American Concrete Institute; 2017. ACI committee 440.

[20] HB 305-2008. Design handbook for RC structures retrofitted with FRP and metal plates: Beams and slabs. Sydney, NSW, Australia: Standard Australia; 2008. Committee BD-101.

[21] D'Antino T, Pellegrino C. Bond between FRP composites and concrete: Assessment of design procedures and analytical models. Compos Part B Eng 2014;60:440–56.

[22] Pan J, Leung CKY, Asce M. Effect of Concrete Composition on FRP / Concrete Bond Capacity 2007;11:611–8.

[23] Barham WS, Obaidat YT, Al-Maabreh AI. Effect of Aggregate Size on the Bond Behavior between Carbon Fiber-Reinforced Polymer Sheets and Concrete. J Mater Civ Eng 2019;31:1–13.

[24] Mukhtar FM. Customized shear test for bond-slip characterization of EBR FRP-concrete system: Influence of substrate aggregate type. Compos Part B Eng 2019;163:606–21.

[25] Chen JF, Li XQ, Lu Y, May IM, Stratford TJ, O'Sullivan R, et al. A new test method for FRP-to-concrete bond behaviour under impact loading. 12th Int. Symp. Struct. Eng., Wuhan: 2012.

[26] GOM Correlate - Precise Industrial 3D Metrology. Braunschweig, Https//www.gom.com.

[27] Wang ZM, Kwan AKH, Chan HC. Mesoscopic study of concrete I: generation of random aggregate structure and finite element mesh. Comput Struct 1999;70:533–44.

[28] Wang X, Yang ZJ, Yates JR, Jivkov AP, Zhang C. Monte Carlo simulations of mesoscale fracture modelling of concrete with random aggregates and pores. Constr Build Mater 2015;75:35–45.

[29] Huang YJ, Yang ZJ, Liu GH, Chen XW. An efficient FE–SBFE coupled method for mesoscale cohesive fracture modelling of concrete. Comput Mech. 2016；58(4):635-55.

[30] Contrafatto L, Cuomo M, Gazzo S. A concrete homogenisation technique at meso-scale level accounting for damaging behaviour of cement paste and aggregates. Comput Struct 2016;173:1–18.

[31] Eurocode 2: Design of concrete structures. London, UK: British Standard; 2004, British Standard Institution.

[32] Mori T, Tanaka K. Average stress in matrix and average elastic energy of materials with misfitting inclusions. Acta Metall 1973;21:571–4.

[33] Tan H, Huang Y, Liu C, Geubelle PH. The Mori-Tanaka method for composite materials with nonlinear interface debonding. Int J Plast 2005;21:1890–918.

[34] Sideris KK, Manita P, Sideris K. Estimation of ultimate modulus of elasticity and Poisson ratio of normal concrete. Cem Concr Compos 2004;26:623–31.

[35] CEB-FIP. CEB-FIB model code. Committee euro-international du beton, lausanne. London: Thomas Telford Services Ltd.; 1991.

[36] BS 8110. Structural Use of Concrete - Part 1: Code of Practice for Design and Construction. London, UK: British Standard; 1997, British Standards Institution.

[37] Hirsch TJ. Modulus of elasticity iof concrete affected by elastic moduli of cement paste matrix and aggregate. In Journal proceedings 1962;59(3):427-452.

[38] An FC, Liu W, Fu B. A predictive 2D finite element model for modelling FRP-to-concrete bond behavior. Compos Struct. 2019;15;226:111189.

[39] Huang YJ, Yang Z, Ren W, Liu G, Zhang C. 3D meso-scale fracture modelling and validation of concrete based on in-situ X-ray Computed Tomography images using damage plasticity model. Int J Solids Struct 2015;67–68:340–52.

[40] Huang YJ, Yang ZJ, Chen XW, Liu GH. Monte Carlo simulations of meso-scale dynamic compressive behavior of concrete based on X-ray computed tomography images. Int J Impact Eng 2016;97:102–15.

[41] Hordijk DA. Local approach to fatigue of concrete PhD thesis Delft: Delft University of Technology; 1991.

[42] Nakamura H, Higai T. Compressive fracture energy and fracture zone length of concrete. Model Inelast Behav RC Struct under Seism Loads 2001:471–87.

[43] Vonk RA. Softening of concrete loaded in compression PhD Thesis Eindhoven: Eindhoven University of Technology; 1992.

[44] Markeset G, Hillerborg A. Softening of concrete in compression-Localization and size effects. Cem Concr Res, 1995;25(4):702–8.

[45] Li X, Chen, JF, Lu Y, & Yang Z. Modelling static and dynamic FRP-concrete bond behaviour using a local concrete damage model. Adv Civ Eng 2015;18(1):45–58.

[46] Alfarah B, López-Almansa F, Oller S. New methodology for calculating damage variables evolution in Plastic Damage Model for RC structures. Eng Struct 2017;132:70-86.

[47] Lubliner J, Oliver J, Oller S, Oñate E. A plastic-damage model for concrete. Int J Solids Struct 1989;25:299–326.